

Cite this: DOI: 10.1039/xxxxxxxxxx

## Ultrafast Charge Transfer and Carrier Dynamics in a WS<sub>2</sub>/MoSe<sub>2</sub> Few-Layer van der Waals Heterostructure

Ang Bian,<sup>a</sup> Shaohua Fu,<sup>a</sup> Pengzhi Wang,<sup>a</sup> Kun Zhao,<sup>a</sup> Jiaqi He,<sup>b</sup> Xiaoxian Zhang,<sup>a</sup> Dawei He,<sup>\*a</sup> Yongsheng Wang,<sup>\*a</sup> and Hui Zhao<sup>\*c</sup>

Received Date

Accepted Date

DOI: 10.1039/xxxxxxxxxx

www.rsc.org/journalname

Photocurrent dynamics including interlayer charge transfer and intralayer valley scattering are studied in a heterostructure formed by trilayers of WS<sub>2</sub> and MoSe<sub>2</sub>. The sample is fabricated by mechanical exfoliation and dry transfer and characterized by atomic force microscopy, Raman spectroscopy, and photoluminescence measurements. The conduction band minima of the two materials are nearly degenerate, representing a unique band alignment. Layer-selective pump-probe measurements are performed with three configurations to reveal a complete picture of the photocurrent dynamics. By comparing the heterostructure with the two individual trilayer materials in each experimental configuration, ultrafast interlayer charge transfer is unambiguously observed, which occurs on the same time scale as the intralayer valley scattering of the photocurrents. The quasi-equilibrium distribution of electrons in the two layers mediate fast carrier recombination process. These results show that the band structure of the few-layer transition metal dichalcogenides can enable rich photocurrent dynamics with intermediate band alignments that are complementary to the previously studied monolayer-monolayer heterostructures.

### Introduction

As a new form of artificial material, two-dimensional (2D) heterostructures have drawn considerable attention since 2013.<sup>1–3</sup> The van der Waals interlayer interaction relaxes the lattice matching restriction, allowing arbitrary combination of 2D materials. The physical properties, in particular electronic and optical properties, of such multilayer heterostructures can be tuned by material choice, layer sequence, and twist angle between different layers. With potentially hundreds of 2D materials as building blocks,<sup>4</sup> this approach could transform material discovery and produce vast number of new functional materials.

Previously, most research efforts have focused on combining two monolayer (1L) materials. Such 1L/1L combinations represent the thinnest possible 2D heterostructures and are ideal platforms to study interface science.<sup>5,6</sup> More recently, however, heterostructures formed by few-layer 2D semiconductors have

drawn some attention. For example, few-layer transition metal dichalcogenides (TMDs) are interesting materials as the weakly coupled layers confined by the van der Waals interface barrier can naturally form multiple-quantum-well structures, as recently demonstrated experimentally.<sup>7,8</sup> Study of few-layer heterostructures can provide several new elements to better understand and apply such materials. First, a 1L TMD can only capture about 15 % of incident light,<sup>9</sup> due to their small thickness. Hence, utilizing few-layers can improve light absorption.<sup>10,11</sup> Second, due to their indirect band structure, few-layer heterostructures can offer rich carrier dynamics involving intralayer and interlayer valley transfer, and thus provide additional knobs to control the carrier dynamics. Third, the finite thickness of few-layers can allow formation of space-charge regions, thus providing a conceptual connection to the traditional 3D heterojunctions. Recently, various devices taking advantage of the few-layer 2D heterostructures have been demonstrated, such as photodetectors,<sup>12–15</sup> transistors,<sup>16</sup> memory<sup>17</sup> and logic devices,<sup>18</sup> as well as photovoltaic devices.<sup>19</sup>

Here we report a time-resolved study on photocurrent dynamics in a model few-layer heterostructure formed by trilayer (3L) WS<sub>2</sub> and MoSe<sub>2</sub>. Our motivation of using 3Ls is two fold. First, the electronic band structure of a 3L TMD is similar to its thicker films and bulk form. Hence, they can mimic carrier dynamics in bulk while still maintaining the important contribution from the interface. Second, with a total of 6 layers, such heterostructures

<sup>a</sup> Key Laboratory of Luminescence and Optical Information, Ministry of Education, Institute of Optoelectronic Technology, Beijing Jiaotong University, Beijing 100044, China. E-mail: dwhe@bjtu.edu.cn; yshwang@bjtu.edu.cn

<sup>b</sup> College of Mathematics and Physics, Beijing University of Chemical Technology, Beijing 100029, China

<sup>c</sup> Department of Physics and Astronomy, The University of Kansas, Lawrence, Kansas 66045, USA. E-mail: huizhao@ku.edu

† Electronic Supplementary Information (ESI) available: Additional data on pump-fluence and probe-wavelength dependence of the differential reflectance signal in the heterostructure sample (PDF).

can enhance light absorption compared to 1L/1L heterostructures, and thus are optimal for light capture or detection applications. Layer-selective pump-probe measurements with three configurations reveal unambiguous evidence of ultrafast interlayer charge transfer (CT), which occurs on the same time scale as the intralayer valley scattering of the photocarriers. The quasi-equilibrium distribution of electrons in the two layers mediate fast carrier recombination process.

## Experimental

The heterostructure sample is obtained by a dry transfer procedure that is carried out at ambient condition.<sup>11,20</sup> Few-layer flakes of MoSe<sub>2</sub> and WS<sub>2</sub> are first peeled off from their bulk crystals by adhesive tapes and transferred to polydimethylsiloxane (PDMS) substrates. The flakes are examined under an optical microscope to assess their size, uniformity, and thickness. A selected MoSe<sub>2</sub> flake is transferred to a Si/SiO<sub>2</sub> substrate by lowering the PDMS substrate (with the flake facing down) onto the Si/SiO<sub>2</sub> substrate, and then lifting up. The same procedure is repeated with a selected WS<sub>2</sub> flake, so that it partially covers the MoSe<sub>2</sub> flake. The sample is annealed in a 100 sccm H<sub>2</sub>/Ar environment at 200° C for 2 hrs.

The transient absorption measurements are performed with a homemade system based on a mode-locked Ti-doped sapphire laser.<sup>21</sup> Together with an optical parametric oscillator, a photonic-crystal supercontinuum generator, and a second-harmonic generation unit, the system produces 100-fs pulses at 80 MHz repetition rate, covering a wavelength range of 410 - 820 nm. For each measurement, two wavelength components are selected as the pump and probe pulses, respectively. They are combined by a beamsplitter and co-focused to the sample surface with a spot size of about 1.8 μm. The sample surface and the overlap of the pump and probe spots are monitored by using a built-in microscope. The reflected probe is detected by a silicon photodiode and a lock-in amplifier. By modulating the pump beam with a mechanical chopper at about 3 kHz, the lock-in amplifier measures the differential reflectance of the probe, which is defined as  $\Delta R/R_0 = (R - R_0)/R_0$ , where  $R$  and  $R_0$  are the probe reflectance from the sample without and with the pump beam being blocked by the chopper, respectively. The sample is kept in ambient condition at room temperature in all measurements.

## Results and discussion

Figure 1(a) shows schematically the heterostructure sample studied, where a 3L WS<sub>2</sub> covers a 3L MoSe<sub>2</sub>. Figure 1(b) presents part of the electronic band structures of the 3L MoSe<sub>2</sub> and 3L WS<sub>2</sub>, according to a recent DFT and GW calculation.<sup>22</sup> The left hexagon illustrates the first Brillouin zone of a hexagonal lattice with the high symmetry points of  $\Gamma$  and  $K$ .  $T$  is a point between  $\Gamma$  and  $K$ .<sup>22</sup> The band extremes of each material only occurs in these valleys, and hence only these valleys are plotted schematically. The numbers indicate the position of the band extremes in eV with respect to the vacuum level. Clearly, for each material, the conduction band minimum (CBM) and valence band maximum (VBM) are at  $T$  and  $\Gamma$  points, respectively. To obtain the band alignment of the heterostructure, we adopt Anderson's rule,<sup>23</sup> which assumes that

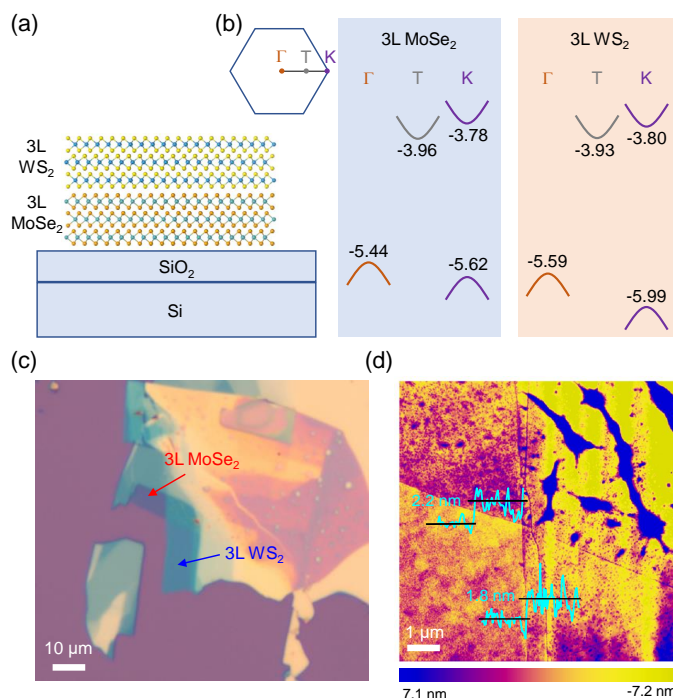


**Fig. 1** (a) Schematics of the crystalline structure of the heterostructure of 3L-WS<sub>2</sub>/3L-MoSe<sub>2</sub>. (b) The electronic band structure of the heterostructure sample. (c) Optical microscope image of the heterostructure sample. (d) Atomic force microscope image of the sample showing thickness of 2.2 and 1.8 nm for the MoSe<sub>2</sub> and WS<sub>2</sub> regions, respectively.

a same vacuum level applies to both sides and the band structure of each material is unaffected by the other layer. Although in principle the screening effect could increase the ionization energy and decrease the electron affinity, the effect on both materials is expected to be similar<sup>22</sup> since they have comparable dielectric responses. Hence, its impact on the band alignment is expected to be insignificant. With these considerations, the global VBM is at the  $\Gamma$  point of MoSe<sub>2</sub>, while that of CBM is at the  $T$  point of MoSe<sub>2</sub>.

We note that the simple model shown in Figure 1(b) does not fully capture realistic band structure of this heterostructure due to two issues. First, the electron-hole interaction is not included in the calculation, which are known to shift the energy of each valley. Second, the interlayer coupling is not considered, which could give rise to hybridization of some of the states to various degrees. Sophisticated and expensive calculations are necessary to accurately capture the band structure of this heterostructure, which is beyond the scope of this experimental study. However, this model is sufficient to discuss various potential electron transfer pathways studied.

Figure 1(c) shows an optical microscopy image of the sample. The individual 3L MoSe<sub>2</sub> and WS<sub>2</sub> regions are indicated by the red and blue arrows, respectively. Their overlapping region is the heterostructure, with a lateral dimension of about 6.5 μm, which is large enough for optical measurements. The thermal annealing procedure is critical for obtaining a good interface, through a self-cleaning mechanism where the van der Waals force pushes the interface contaminants into bubble-like structures,<sup>24</sup> which

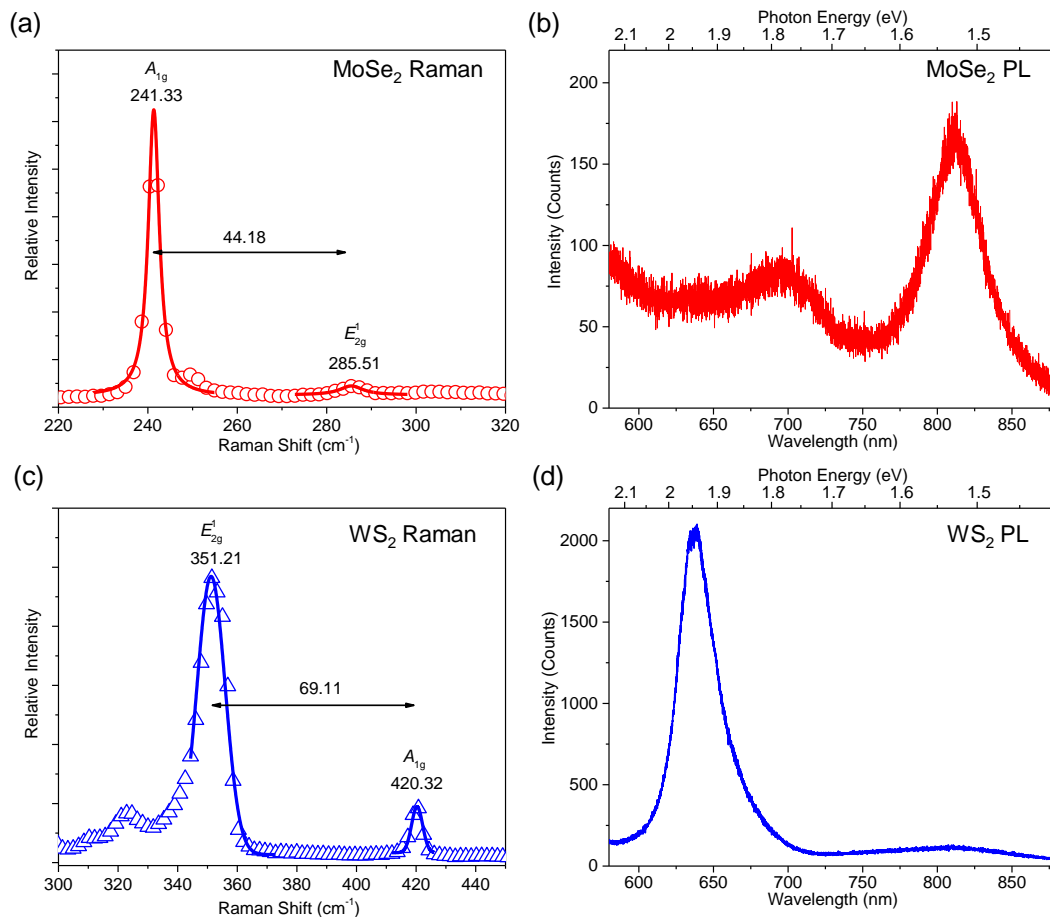


**Fig. 2** Raman and photoluminescence (PL) spectra of the individual regions of MoSe<sub>2</sub> (a, b) and WS<sub>2</sub> (c, d), respectively, all obtained with 2.33-eV and 0.7 mW cm<sup>-2</sup> continuous-wave excitation. Curves in (a) and (c) are fits to determine the peak positions.

can be seen in the heterostructure region but not from individual MoSe<sub>2</sub> and WS<sub>2</sub> regions [Fig. 1(c)]. The areas of the heterostructure that are free of bubbles thus acquire an atomically clean interface.<sup>25,26</sup> Figure 1(d) is the height profile of an atomic force microscope (AFM) image. The thicknesses of the MoSe<sub>2</sub> and WS<sub>2</sub> flakes are 2.2 and 1.8 nm, respectively, suggesting their 3L thickness according to their 1L thicknesses 0.7 nm<sup>27</sup> and 0.6 nm,<sup>28</sup> respectively.

To further confirm the thickness of the MoSe<sub>2</sub> and WS<sub>2</sub> flakes, Raman and photoluminescence (PL) spectroscopic measurements are performed. Figure 2(a) shows the Raman spectrum measured from the MoSe<sub>2</sub> region that is not covered by WS<sub>2</sub>. It shows two characteristic peaks at 241.33 and 285.51 cm<sup>-1</sup>, corresponding to the A<sub>1g</sub> and E<sub>2g</sub><sup>1</sup> modes, respectively.<sup>29</sup> It has been previously shown that the separation of these two modes is a good indicator of the sample thickness.<sup>30</sup> For MoSe<sub>2</sub>, this separation is 46.5, 44.8, 44.2, and 43.7 cm<sup>-1</sup> for 1, 2, 3, and 4 layers, respectively.<sup>30</sup> Our result of 44.18 cm<sup>-1</sup> agrees well with the 3L value. Figure 2(b) shows the PL spectrum measured from the same region. The peak at about 700 nm is a signature of 3L MoSe<sub>2</sub>, which has been previously observed in 3L MoSe<sub>2</sub> but is absent in the PL spectra of 1, 2, and 4 layers.<sup>30</sup> For the WS<sub>2</sub> flake, previous thickness-dependent Raman spectroscopy measurements have reported the values of peak separation of 65.6, 68.3, 69.2, and 69.9 cm<sup>-1</sup> for

1, 2, 3, and 4 layer WS<sub>2</sub>, respectively.<sup>31</sup> Our result of 69.11 cm<sup>-1</sup>, as shown in Figure 2(c), agrees well with the 3L value. Finally, previous PL measurements of few-layer WS<sub>2</sub> have established an indirect transition with PL peaks at about 720, 810, 845, and 870 nm for 2, 3, 4, and 5 layers, respectively (which is absent in 1L).<sup>32</sup> The weak peak we observed at about 815 nm is consistent with the 3L value. Hence, these Raman and PL results, along with the AFM data, well establish that both flakes are 3Ls.

The photocarrier dynamics and interlayer CT are studied by transient absorption measurements. In the first configuration, we use a 1.57-eV pump pulse to excite excitons that are composed of electrons (-) and holes (+) in the K valley of 3L MoSe<sub>2</sub>, as indicated by the blue vertical arrow in Figure 3(a). The photon energy is insufficient to excite carriers in other valleys of MoSe<sub>2</sub> nor any valley in WS<sub>2</sub>. The excited electrons could transfer to the T valley of the same layer via an intervalley scattering process or to the T valley of WS<sub>2</sub> by interlayer CT. These processes are expected to co-exist, since recent studies have revealed that the intervalley scattering time in such materials is about several hundred femtoseconds,<sup>33,34</sup> which is on the same order of magnitude with the interlayer CT times in TMD heterostructures.<sup>35,36</sup> Since the bottoms of the T valleys of the two layers are nearly degenerate, electrons are expected to populate both valleys. The holes excited in K valley are expected to scattering to the  $\Gamma$  valley of

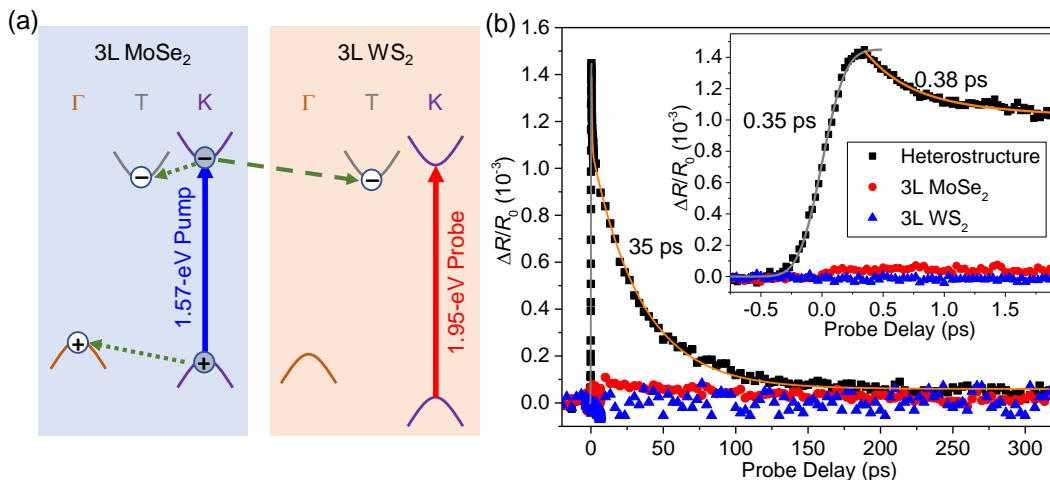


**Fig. 3** (a) Schematics of the band structure and photocarrier dynamics after excitation of electrons (-) and holes (+) in K valley of MoSe<sub>2</sub> by a 1.57-eV pump pulse, including intralayer valley transfer (dotted green arrows) and interlayer CT (dashed green arrow). (b) Differential reflectance of a 1.95-eV probe pulse measured from the heterostructure and the individual 3Ls. The inset shows the data near zero probe delay.

MoSe<sub>2</sub>, which is the global VBM.

To reveal these potential photocarrier dynamic processes, a 1.95-eV probe pulse is used, which is tuned to the K valley optical bandgap of 3L WS<sub>2</sub>, as illustrated by the red arrow in Figure 3(a). Its differential reflectance (DR) is measured as a function of the probe delay. We assume that this quantity measures the carrier density in the WS<sub>2</sub> layer through various mechanisms. Specifically, the electrons and holes, as well as excitons, in K valley could saturate the absorption of the probe *via* phase-space state filling and screening effects, and thus produces a DR signal.<sup>37</sup> Carriers in the  $\Gamma$  and T valleys can also produce a signal *via* screening effect,<sup>38</sup> although they do not occupy the K valley. Given the strong excitonic effect in such 2D systems, the screening effect could be rather significant.<sup>39</sup> On the other hand, we assume that the probe is less sensitive to the carriers in the MoSe<sub>2</sub> layer as they are spatially separated from the WS<sub>2</sub> layer and thus with weaker screening effects.

The black symbols in Figure 3(b) show the DR signal of the 1.95-eV probe measured from the heterostructure sample with a pump pulse fluence of  $4.4 \mu\text{J cm}^{-2}$ , which corresponds to a photon number density of  $1.8 \times 10^{13} \text{ cm}^{-2}$ . By an interference analysis of the 3L-WS<sub>2</sub>/3L-MoSe<sub>2</sub>/SiO<sub>2</sub>/Si multilayer structure<sup>11</sup> using previously reported complex indices of refraction of TMDs,<sup>40</sup> the MoSe<sub>2</sub> layer is estimated to absorb 16 % of the incident photons. Hence, the pump injects K-valley excitons in MoSe<sub>2</sub> with a peak areal density of  $2.9 \times 10^{12} \text{ cm}^{-2}$ . This is a moderate exciton density, since it is much higher than the expected defect density of the materials but too low for the onset of the multi-exciton processes such as exciton-exciton annihilation<sup>41,42</sup> and biexciton formation,<sup>43</sup> with an average distance between excitons of about 6 nm. Since the WS<sub>2</sub> layer is not excited, the observed DR signal, with a magnitude on the order of  $10^{-3}$ , suggests the existence of interlayer CT process from the K valley of MoSe<sub>2</sub> to the T valley of WS<sub>2</sub>, as depicted by the dashed green arrow in Figure 3(a). To confirm this interpretation, the same measurement is done on the individual 3L-WS<sub>2</sub> region of the sample, which produces no signal

(blue symbols). This demonstrates that the pump does not excite the 3L WS<sub>2</sub>, and therefore the signal observed in the heterostructure must originate from the carriers that are excited in MoSe<sub>2</sub> and subsequently transferred to WS<sub>2</sub>. Similarly, the same measurement on the individual 3L-MoSe<sub>2</sub> region produces a much weaker signal (red symbols), confirming that the probe mainly senses the transient absorption of the WS<sub>2</sub> layer. Furthermore, by tuning the probe photon energy, we confirm that the signal from the heterostructure depends strongly on the photon energy near the K-valley exciton resonance of WS<sub>2</sub> (Figure ESI1), which is consistent with its PL spectrum. This feature rules out the possibility that the probe sensed the higher states of the MoSe<sub>2</sub> layer.

Since the signal monitors the carrier density in the WS<sub>2</sub> layer, its temporal evolution reflects the interlayer CT and carrier dynamics in the heterostructure. As shown in the inset of Figure 3(b), the rise of the DR signal can be fit by the integral of a Gaussian function with a full width at half maximum of 0.35 ps (gray curve). This time is close to the cross-correlation of the pump and probe pulses (and thus the time resolution of the measurement), indicating that the appearance of carriers in WS<sub>2</sub> due to the interlayer CT process occurs on a much shorter time scale of 0.1 ps or less. Previously, ultrafast CT in heterostructures formed by TMD 1Ls has been widely observed by using various experimental techniques, including time-resolved transient absorption,<sup>35,36,44,45</sup> THz radiation,<sup>46</sup> second harmonic generation,<sup>47</sup> and angle-resolved photoemission,<sup>34</sup> as well as steady-state measurements of PL quenching,<sup>48–50</sup> PL excitation,<sup>51</sup> and absorption spectroscopy.<sup>52</sup> Here, the observed similarly fast CT in our 3L/3L heterostructure is encouraging news for developing few-layer heterostructures with novel CT properties. In 1L/1L heterostructures, the CT was thought to be driven by the coherent lattice oscillation between the 1Ls.<sup>53–55</sup> Our results suggest that such processes could remain effective between 3Ls.

The decay of the signal shown in Figure 3(b) is fit by a bi-exponential function,  $\Delta R/R_0 = A_1 \exp(-t/\tau_1) + A_2 \exp(-t/\tau_2) + B$ , as shown by the orange curve. The  $\tau_1$  ( $0.38 \pm 0.05$  ps, which ac-

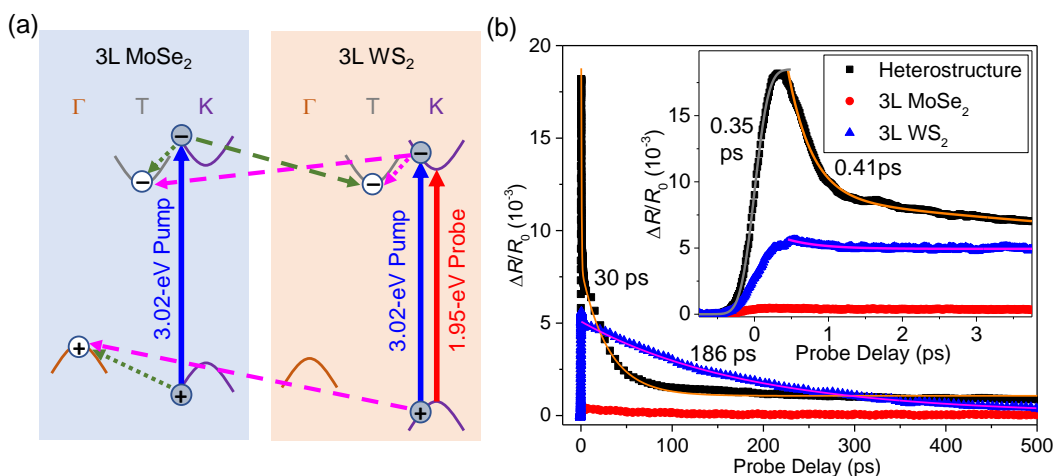


**Fig. 4** (a) Schematics of the band structure and photocarrier dynamics after excitation of electrons (-) and holes (+) in K valley of both MoSe<sub>2</sub> and WS<sub>2</sub> layers by a 3.02-eV pump pulse, including those initiated in MoSe<sub>2</sub> (green arrows) and those from WS<sub>2</sub> (pink arrows). (b) Differential reflectance of a 1.95-eV probe pulse measured from the heterostructure and its individual 3Ls. The inset shows the data near zero probe delay.

counts for about 25 % of the signal) process could be associated with the formation process of interlayer excitons of the T-valley electrons in WS<sub>2</sub> and the  $\Gamma$ -valley holes in MoSe<sub>2</sub>. The  $\tau_2$  ( $35 \pm 3$  ps) process (with a 75 % weight) is assigned to the recombination of these interlayer excitons. By repeating the measurement with various pump fluences (Figure ESI2), it was found that the peak signal is proportional to the pump fluence (and thus the injected carrier density), while the rise and decay time constants are independent of the pump fluence, confirming that the measurement is performed in the moderate carrier density regime.

To further study the photocarrier dynamics and interlayer CT processes in this heterostructure, we next change the pump photon energy to 3.02 eV, which is enough to excite the K valleys of both layers. As schematically shown in Figure 4(a), in addition to the transfer pathways of the carriers injected in the K valley of MoSe<sub>2</sub> (green arrows), the electrons excited in the K valley of WS<sub>2</sub> can scatter to its T valley or transfer to the T valley of MoSe<sub>2</sub> via interlayer CT, while the K-valley holes in WS<sub>2</sub> can transfer to the  $\Gamma$  valley of MoSe<sub>2</sub> (pink arrows). The final carrier population is composed of electrons in the T valleys of both layers and holes residing in the  $\Gamma$  valley of MoSe<sub>2</sub>. The same 1.95-eV probe is used to monitor the carrier population in WS<sub>2</sub>. The black symbols in Figure 4(b) show the DR signal with a pump fluence of  $4.4 \mu\text{J cm}^{-2}$ , which injects peak carrier densities of 6 and  $2 \times 10^{12} \text{ cm}^{-2}$  in the WS<sub>2</sub> and MoSe<sub>2</sub> layers, respectively, due to the large absorption coefficients of the two materials at 3.02 eV.<sup>40</sup> Similar to the results with the 1.57-eV pump, the rise time of the signal is the resolution-limited 0.35 ps (gray curve) while the decay of the signal is biexponential (orange curve) with  $\tau_1 = 0.41 \pm 0.05$  ps (with a weight of 60 %) and  $\tau_2 = 30 \pm 2$  ps (40 %).

To understand these features, we first discuss the DR signal from the 3L-WS<sub>2</sub> region of the sample under this pump-probe configuration, as shown by the blue symbols in Figure 4(b). The signal decays single-exponentially with a time constant of  $186 \pm 15$  ps. We can attribute this process to the recombination of the excitons in 3L-WS<sub>2</sub> formed by the T-valley electrons and the  $\Gamma$ -valley

holes. Based on this result, we can assign the 0.41-ps decay process of the heterostructure ( $\tau_1$ ), which is absent in the individual WS<sub>2</sub> 3L, to the transfer of the electrons from the K valley of WS<sub>2</sub> to the T-valley of MoSe<sub>2</sub> and that of the holes from the K valley of WS<sub>2</sub> to the  $\Gamma$  valley of MoSe<sub>2</sub> (pink dashed arrows), since both processes result in net loss of the carrier population in WS<sub>2</sub>. The intralayer electron transfer from the K valley to the T valley of WS<sub>2</sub> (pink dotted arrow) is expected to happen on the same time scale; however, it does not result in significant decrease of the signal since this process should similarly happen in the individual 3L WS<sub>2</sub> sample, too. After these fast transfer processes, the DR signal from the heterostructure monitors the population of the T valley electrons of WS<sub>2</sub>, and its decay is due to their recombination with the holes in the  $\Gamma$  valley of MoSe<sub>2</sub>. The 30-ps time constant is slightly shorter than the results obtained with the 1.57-eV pump, which could be due to the higher carrier density here. Indeed, by repeating the measurement with various pump fluences (see Figure ESI3), we find that the signal is proportional to the pump fluence, while the decay time constant decreases with it. Finally, the same measurement performed on the 3L-MoSe<sub>2</sub> region produced a much weaker signal (red symbols), since the probe is far away from the optical bandgap of MoSe<sub>2</sub>. This further confirms our above interpretation of the photocarrier dynamics in the heterostructure.

Finally, we use a configuration shown in Figure 5, with pump and probe photon energies of 2.25 and 1.57 eV, respectively. The pump pulse still excites carriers in the K valleys of both layers. Hence, the photocarrier dynamics is expected to be similar to those studied with the previous configuration shown in Figure 4(a). However, here, the probe monitors the carriers in MoSe<sub>2</sub> layer as it is tuned to its K-valley bandgap [red arrow in Figure 5(a)]. Therefore, the DR signal monitors the density of carriers in MoSe<sub>2</sub>, providing complementary information to the previous configuration. As shown by the black symbols, the signal rise is slower than the previous configurations, with a full width at half maximum (Gauss integral) of  $0.87 \pm 0.10$  ps (gray curve).

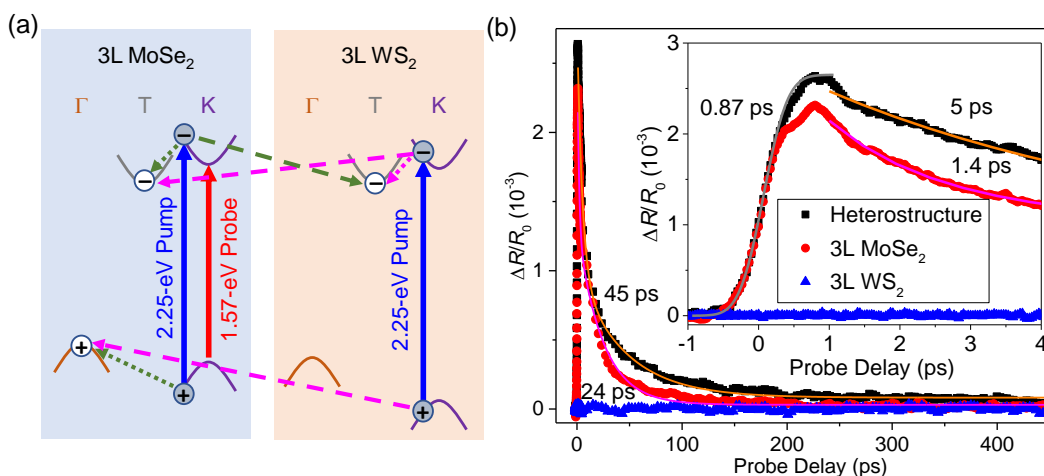


**Fig. 5** (a) Schematics of the band structure and photocarrier dynamics after excitation of electrons (-) and holes (+) in K valley of both MoSe<sub>2</sub> and WS<sub>2</sub> layers by a 2.25-eV pump pulse. (b) Differential reflectance of a 1.57-eV probe pulse measured from the heterostructure and its individual constituents.

The decay is biexponential (orange curve) with  $\tau_1 = 5 \pm 1$  ps and  $\tau_2 = 45 \pm 3$  ps, with weight of 60 % and 40 %, respectively. By tuning the probe photon energy, we confirm that the signal indeed originates from transient absorption associated with the K-valley exciton states in MoSe<sub>2</sub> (Figure ESI4). Furthermore, by change the pump fluence, the DR signal is found to be proportional to the pump fluence for low fluences and then show a saturation effect at elevated fluences (Figure ESI5). The decay is independent of the pump fluence (Figure ESI5). The same measurement performed on the 3L-MoSe<sub>2</sub> region produces a signal with a similar magnitude and rise time (red symbols), with two decay time constants are  $1.4 \pm 0.2$  ps (40 %) and  $24 \pm 2$  ps (60 %). Hence, the 0.87-ps rise process is due to intralayer carrier dynamics in MoSe<sub>2</sub> and is unrelated to interlayer CT. The control experiment performed on the 3L-WS<sub>2</sub> region yields no signal (blue symbols), as the probe is below its direct bandgap.

The three configurations used above have established ultrafast interlayer CT in the 3L-MoSe<sub>2</sub>/3L-WS<sub>2</sub> heterostructure. As in previously studied heterostructures formed by 1Ls, one consequence of CT is the formation of the interlayer excitons with electrons and holes that are spatially separated. Figure 6 summarizes the carrier distribution after the ultrafast transients in each individual material and their heterostructure. For the individual 3L MoSe<sub>2</sub>, the K-valley electrons and holes transfer to the T and  $\Gamma$  valleys, respectively, and form excitons that are spatially overlapped but are indirect in momentum space. Their recombination lifetime is  $24 \pm 2$  ps, according to our data. Similarly, in the 3L WS<sub>2</sub>, such excitons have a lifetime of  $186 \pm 15$  ps. In both cases, the recombination lifetimes are limited by the nonradiative recombination, since the radiative recombination lifetime of such indirect excitons are expected to be several nanoseconds.<sup>56</sup> The difference between the two lifetimes could reflect their different crystalline quality (defect density). In the heterostructure, the T valley of both layers are occupied by the electrons after the interlayer CT process, while the holes populate the  $\Gamma$  valley of MoSe<sub>2</sub>. The overall lifetime of these carriers is in the range of 30 - 45 ps. We hypothesize that the recombination process here is mediated by

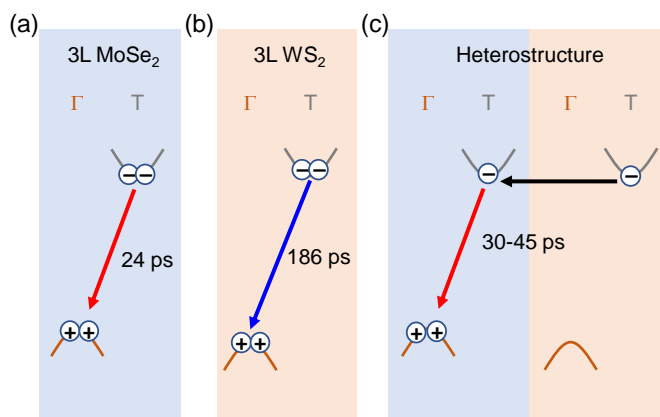


**Fig. 6** Schematics of the exciton recombination dynamics in 3L MoSe<sub>2</sub> (a), 3L WS<sub>2</sub> (b), and their heterostructure (c).

transfer of the electrons from the T valley of WS<sub>2</sub> to the T valley of MoSe<sub>2</sub>, followed by their recombination with the holes in the  $\Gamma$  valley of MoSe<sub>2</sub>.

## Conclusions

In summary, transient absorption measurements revealed rich photocarrier dynamics in a heterostructure formed by 3Ls of WS<sub>2</sub> and MoSe<sub>2</sub>. Such a heterostructure, with a total thickness of 6 monolayers, is attractive for photovoltaic and photodetection applications due to its large overall light absorbance. With nearly degenerate K and T valleys of both layers, this heterostructure provides an intriguing system that bridges type-I and type-II band alignments. Time-resolved measurements with three experimental configurations show unambiguous evidence of interlayer CT processes that can be initiated in each layer. The quasi-equilibrium distribution of the electrons in the two T valleys mediates fast carrier recombination process. These results show that the band structure of the few-layer TMDs can enable rich photocarrier dynamics with intermediate band alignments that are complementary to the previously studied 1L/1L heterostructures.

## Author contributions

Ang Bian: data curation (lead); methodology (lead); formal analysis (lead); writing - original draft preparation. Shaohua Fu: data curation (supporting); methodology (supporting). Pengzhi Wang: data curation (supporting); methodology (supporting). Kun Zhao: data curation (supporting); methodology (supporting). Jiaqi He: methodology (supporting); formal analysis (supporting). Xiaoxian Zhang: methodology (supporting); supervision (supporting). Dawei He: conceptualization (equal); supervision (equal); writing - review & editing (equal). Yongsheng Wang: conceptualization (equal); supervision (equal); writing - review & editing (equal); funding acquisition (lead). Hui Zhao: conceptualization (equal); supervision (equal); writing - review & editing (equal); validation (lead).

## Acknowledgment

Yongsheng Wang and Dawei He are grateful to acknowledge the financial support from National Natural Science Foundation of China (nos 61875236 and 61975007) and Beijing Natural Science Foundation of China (no Z190006). Jiaqi He acknowledges the financial support from National Natural Science Foundation of China (no 61905010). Xiaoxian Zhang acknowledges the financial support from National Nature Science Foundation of China (no 11974088). Ang Bian received funding from the Fundamental Research Funds for the Central Universities of China (Beijing Jiaotong University, no 2020YJS176). Hui Zhao is supported by the U.S. Department of Energy, Office of Basic Energy Sciences, Division of Materials Sciences and Engineering under Award DE-SC0020995.

## Conflicts of interest

There are no conflicts to declare.

## References

- 1 A. K. Geim and I. V. Grigorieva, *Nature*, 2013, **499**, 419–425.
- 2 P. Rivera, H. Y. Yu, K. L. Seyler, N. P. Wilson, W. Yao and X. D. Xu, *Nat. Nanotechnol.*, 2018, **13**, 1004–1015.
- 3 J. J. Linghu, T. Yang, Y. Z. Luo, M. Yang, J. Zhou, L. Shen and Y. P. Feng, *ACS Appl. Mater. Interfaces*, 2018, **10**, 32142–32150.
- 4 N. Mounet, M. Gibertini, P. Schwaller, D. Campi, A. Merkys, A. Marrazzo, T. Sohler, I. E. Castelli, A. Cepellotti, G. Pizzi and N. Marzari, *Nat. Nanotechnol.*, 2018, **13**, 246–252.
- 5 C. H. Jin, E. Y. Ma, O. Karni, E. C. Regan, F. Wang and T. F. Heinz, *Nat. Nanotechnol.*, 2018, **13**, 994–1003.
- 6 K. S. Novoselov, A. Mishchenko, A. Carvalho and A. H. C. Neto, *Science*, 2016, **353**, aac9439.
- 7 P. Schmidt, F. Violla, S. Latini, M. Massicotte, K. J. Tielrooij, S. Mastel, G. Navickaite, M. Danovich, D. A. Ruiz-Tijerina, C. Yelgel, V. Fal'ko, K. S. Thygesen, R. Hillenbrand and F. H. L. Koppens, *Nat. Nanotechnol.*, 2018, **13**, 1035–1041.
- 8 K. Takeyama, R. Moriya, S. Okazaki, Y. Zhang, S. Masubuchi, K. Watanabe, T. Taniguchi, T. Sasagawa and T. Machida, *Nano Lett.*, 2021, **21**, 3929–3934.
- 9 Y. Li, A. Chernikov, X. Zhang, A. Rigosi, H. M. Hill, A. M. van der Zande, D. A. Chenet, E.-M. Shih, J. Hone and T. F. Heinz, *Phys. Rev. B*, 2014, **90**, 205422.
- 10 D. Jariwala, A. R. Dayoyan, G. Tagliabue, M. C. Sherrott, J. Wong and H. A. Atwater, *Nano Lett.*, 2016, **16**, 5482–5487.
- 11 F. Ceballos, P. Zereshki and H. Zhao, *Phys. Rev. Mater.*, 2017, **1**, 044001.
- 12 W. Gao, F. Zhang, Z. Zheng and J. Li, *ACS Appl. Mater. Interfaces.*, 2019, **11**, 19277–19285.
- 13 F. Wu, Q. Li, P. Wang, H. Xia, Z. Wang, Y. Wang, M. Luo, L. Chen, F. S. Chen, J. S. Miao, X. S. Chen, W. Lu, C. X. Shan, A. L. Pan, X. Wu, W. C. Ren, D. Jariwala and W. D. Hu, *Nat. Commun.*, 2019, **10**, 4663.
- 14 C. R. P. Inbaraj, R. J. Mathew, R. K. Ulaganathan, R. Sankar, M. Kataria, H. Y. Lin, H. Y. Cheng, K. H. Lin, H. I. Lin, Y. M. Liao, F. C. Chou, Y. T. Chen, C. H. Lee and Y. F. Chen, *ACS Appl. Mater. Interfaces.*, 2020, **12**, 26213–26221.
- 15 Y. Xin, X. X. Wang, Z. Chen, D. Weller, Y. Y. Wang, L. J. Shi, X. Ma, C. J. Ding, W. Li, S. Guo and R. B. Liu, *ACS Appl. Mater. Interfaces*, 2020, **12**, 15406–15413.
- 16 E. Wu, Y. Xie, Q. Liu, X. Hu, J. Liu, D. Zhang and C. Zhou, *ACS Nano*, 2019, **13**, 5430–5438.
- 17 C. S. Liu, X. Yan, X. F. Song, S. J. Ding, D. W. Zhang and P. Zhou, *Nat. Nanotechnol.*, 2018, **13**, 404–410.
- 18 Y. Hassan, P. K. Srivastava, B. Singh, M. S. Abbas, F. Ali, W. J. Yoo and C. Lee, *ACS Appl. Mater. Interfaces*, 2020, **12**, 14119–14124.
- 19 A. J. Cho, M. K. Song, D. W. Kang and J. Y. Kwon, *ACS Appl. Mater. Interfaces*, 2018, **10**, 35972–35977.
- 20 A. Castellanos-Gomez, M. Buscema, R. Molenaar, V. Singh, L. Janssen, H. S. J. van der Zant and G. A. Steele, *2D Materials*, 2014, **1**, 011002.
- 21 X. Han, X. Liang, D. He, L. Jiao, Y. Wang and H. Zhao, *ACS Appl. Mater. Interfaces*, 2021, **13**, 44703–44710.
- 22 H. Kim and H. J. Choi, *Phys. Rev. B*, 2021, **103**, 085404.
- 23 R. L. Anderson, *IBM J. Res. Dev.*, 1960, **4**, 283–287.
- 24 S. J. Haigh, A. Gholinia, R. Jalil, S. Romani, L. Britnell, D. C. Elias, K. S. Novoselov, L. A. Ponomarenko, A. K. Geim and R. Gorbachev, *Nat. Mater.*, 2012, **11**, 764–767.
- 25 D. G. Purdie, N. M. Pugno, T. Taniguchi, K. Watanabe, A. C. Ferrari and A. Lombardo, *Nat. Commun.*, 2018, **9**, 5387.
- 26 Y. Kim, P. Herlinger, T. Taniguchi, K. Watanabe and J. H. Smet, *ACS Nano*, 2019, **13**, 14182–14190.
- 27 X. Li, A. A. Purotzky, X. Sang, S. Kc, M. Tian, F. Ceballos, M. Mahjouri-Samani, K. Wang, R. R. Unocic, H. Zhao, G. Duscher, V. R. Cooper, C. M. Rouleau, D. B. Geohegan and K. Xiao, *Adv. Funct. Mater.*, 2017, **27**, 1603850.
- 28 H. R. Gutierrez, N. Perea-Lopez, A. L. Elias, A. Berkdemir, B. Wang, R. Lv, F. Lopez-Urias, V. H. Crespi, H. Terrones and M. Terrones, *Nano Lett.*, 2013, **13**, 3447–3454.
- 29 A. A. Purotzky, L. B. Liang, X. F. Li, K. Xiao, K. Wang, M. Mahjouri-Samani, L. Basile, J. C. Idrobo, B. G. Sumpter, V. Meunier and D. B. Geohegan, *ACS Nano*, 2015, **9**, 6333–6342.

- 30 K. Kim, J. U. Lee, D. Nam and H. Cheong, *ACS Nano*, 2016, **10**, 8113–8120.
- 31 H. Zeng, G.-B. Liu, J. Dai, Y. Yan, B. Zhu, R. He, L. Xie, S. Xu, X. Chen, W. Yao and X. Cui, *Sci. Rep.*, 2013, **3**, 1608.
- 32 W. J. Zhao, Z. Ghorannevis, L. Q. Chu, M. L. Toh, C. Kloc, P. H. Tan and G. Eda, *ACS Nano*, 2013, **7**, 791–797.
- 33 J. Madéo, M. K. L. Man, C. Sahoo, M. Campbell, V. Pareek, E. L. Wong, A. Al-Mahboob, N. S. Chan, A. Karmakar, B. M. K. Mariserla, X. Li, T. F. Heinz, T. Cao and K. M. Dani, *Science*, 2020, **370**, 1199–1204.
- 34 F. Liu, Q. Y. Li and X. Y. Zhu, *Phys. Rev. B*, 2020, **101**, 201405(R).
- 35 X. Hong, J. Kim, S. F. Shi, Y. Zhang, C. Jin, Y. Sun, S. Tongay, J. Wu, Y. Zhang and F. Wang, *Nat. Nanotechnol.*, 2014, **9**, 682–686.
- 36 F. Ceballos, M. Z. Bellus, H. Y. Chiu and H. Zhao, *ACS Nano*, 2014, **8**, 12717–12724.
- 37 F. Ceballos and H. Zhao, *Adv. Funct. Mater.*, 2017, **27**, 1604509.
- 38 S. Schmitt-Rink, D. S. Chemla and D. A. B. Miller, *Phys. Rev. B*, 1985, **32**, 6601–6609.
- 39 S. Y. Gan, Y. F. Liang, C. D. Spataru and L. Yang, *Nano Lett.*, 2016, **16**, 5568–5573.
- 40 H.-L. Liu, C.-C. Shen, S.-H. Su, C.-L. Hsu, M.-Y. Li and L.-J. Li, *Appl. Phys. Lett.*, 2014, **105**, 201905.
- 41 N. Kumar, Q. Cui, F. Ceballos, D. He, Y. Wang and H. Zhao, *Phys. Rev. B*, 2014, **89**, 125427.
- 42 D. Sun, Y. Rao, G. A. Reider, G. Chen, Y. You, L. Brezin, A. R. Harutyunyan and T. F. Heinz, *Nano Lett.*, 2014, **14**, 5625–5629.
- 43 Y. M. You, X. X. Zhang, T. C. Berkelbach, M. S. Hybertsen, D. R. Reichman and T. F. Heinz, *Nat. Phys.*, 2015, **11**, 477–481.
- 44 L. Yuan, T. F. Chung, A. Kuc, Y. Wan, Y. Xu, Y. P. Chen, T. Heine and L. B. Huang, *Sci. Adv.*, 2018, **4**, e1700324.
- 45 X. W. Wen, H. L. Chen, T. M. Wu, Z. H. Yu, Q. R. Yang, J. W. Deng, Z. T. Liu, X. Guo, J. X. Guan, X. Zhang, Y. J. Gong, J. T. Yuan, Z. H. Zhang, C. Y. Yi, X. F. Guo, P. M. Ajayan, W. Zhuang, Z. R. Liu, J. Lou and J. R. Zheng, *Nat. Commun.*, 2018, **9**, 1859.
- 46 E. Y. Ma, B. Guzelturk, G. Q. Li, L. Y. Cao, Z. X. Shen, A. M. Lindenberg and T. F. Heinz, *Sci. Adv.*, 2019, **5**, eaau0073.
- 47 P. Yao, D. He, P. Zereszki, Y. Wang and H. Zhao, *Appl. Phys. Lett.*, 2020, **115**, 263103.
- 48 H. Fang, C. Battaglia, C. Carraro, S. Nemsak, B. Ozdol, J. S. Kang, H. A. Bechtel, S. B. Desai, F. Kronast, A. A. Unal, G. Conti, C. Conlon, G. K. Palsson, M. C. Martin, A. M. Minor, C. S. Fadley, E. Yablonovitch, R. Maboudian and A. Javey, *Proc. Natl. Acad. Sci. U. S. A.*, 2014, **111**, 6198–6202.
- 49 Y. Gong, J. Lin, X. Wang, G. Shi, S. Lei, Z. Lin, X. Zou, G. Ye, R. Vajtai, B. I. Yakobson, H. Terrones, M. Terrones, B. K. Tay, J. Lou, S. T. Pantelides, Z. Liu, W. Zhou and P. M. Ajayan, *Nat. Mater.*, 2014, **13**, 1135–1142.
- 50 C. H. Lee, G. H. Lee, A. M. van der Zande, W. Chen, Y. Li, M. Han, X. Cui, G. Arefe, C. Nuckolls, T. F. Heinz, J. Guo, J. Hone and P. Kim, *Nat. Nanotechnol.*, 2014, **9**, 676–681.
- 51 D. Kozawa, A. Carvalho, I. Verzhbitskiy, F. Giustiniano, Y. Miyauchi, S. Mouri, A. H. C. Neto, K. Matsuda and G. Eda, *Nano Lett.*, 2016, **16**, 4087–4093.
- 52 A. F. Rigos, H. M. Hill, Y. L. Li, A. Chernikov and T. F. Heinz, *Nano Lett.*, 2015, **15**, 5033–5038.
- 53 H. Wang, J. Bang, Y. Y. Sun, L. B. Liang, D. West, V. Meunier and S. B. Zhang, *Nat. Commun.*, 2016, **7**, 11504.
- 54 Q. J. Zheng, W. A. Saidi, Y. Xie, Z. G. Lan, O. V. Prezhdo, H. Petek and J. Zhao, *Nano Lett.*, 2017, **17**, 6435–6442.
- 55 R. Long and O. V. Prezhdo, *Nano Lett.*, 2016, **16**, 1996–2003.
- 56 Z. Gao, Y. Liu, H. Liu, C. Qiu, S. Zheng and D. Liu, *J. Phys. Chem. C*, 2020, **124**, 21123–21128.